Fuel 353 (2023) 129192

Contents lists available at ScienceDirect

Fuel

journal homepage: www.elsevier.com/locate/fuel

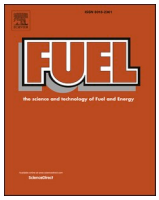

Full Length Article

Investigation of boost pressure and spark timing on combustion and NO emissions under lean mixture operation in hydrogen engines

D.N. Rrustemi, L.C. Ganippa, C.J. Axon *

Department of Mechanical and Aerospace Engineering, Brunel University London, Uxbridge, London UB8 3PH, UK

A B S T R A C T

Hydrogen may become a replacement for liquid fossil fuels, contributing to greenhouse gas emissions reductions by improving the thermal efficiency of boosted lean burn spark ignition engines. Single-zone engine combustion models are simple, but can yield useful results as a step in the design process for developing alternative fuel systems. The single-zone thermodynamic model is advanced by implementing a laminar flame speed sub-model to investigate combustion, an extended Zeldovich mechanism for nitric oxide emissions, and incorporating the Livengood-Wu integral model for knock characteristics. The results were validated using published experiments giving satisfactory predictions between simulation and experiment for spark timing variation, manifold air pressure, and equivalence ratios. A detailed analysis of boosted lean burn strategies showed that nitric oxide emissions increased with boosted pressure, hence emissions can be controlled through optimizing the excess air ratio and the start of combustion. Further techniques to achieve high thermal efficiency and to prevent knock for boosted lean burn hydrogen SI engine are discussed.

1. Introduction and background

Hydrogen is expected to be important for meeting CO_2 emissions reduction targets [1] as it has the potential to be a clean energy carrier for use in internal combustion engines (ICE) by improving thermal efficiency and performance [2–4]. Modelling is an important step of the design process for using alternative fuels in ICEs. Due to its high auto-ignition temperature, hydrogen is better suited to spark ignition (SI) engines than compression ignition (CI) engines [5]. Mathematical models based on single-zone, two-zone, or multi-zone models to predict combustion processes of the ICE have been developed. Yet, models require experimentally validated combustion data to obtain reasonable accuracy. Theoretical modelling of SI engines for conventional fuels is well-established but is lacking for hydrogen.

There are several advantages of using hydrogen in SI engines (Table 1), 1) the laminar flame speed of hydrogen is more than four times greater than that of gasoline; 2) the diffusion coefficient is more than three times greater, enhancing the mixing of the fuel and air (resulting in improved homogeneity); 3) the lean limit is much lower, meaning that hydrogen engines can operate stably with lean burn mixtures (providing an effective path towards improving the thermal efficiency); 4) the higher Research Octane Number (RON) potentially offers a higher knock resistance [6].

The current limitations of pure hydrogen SI engines are low volumetric energy, high levels of NOx emissions and low ignition energy [2–4,7]. Since a hydrogen–air mixture has lower volumetric energy, the operation of naturally aspirated hydrogen SI engines could lead to a performance reduction. Berckmüller et al. [8] showed that by charging the intake pressure of a hydrogen SI engine, the same level of performance as a standard gasoline engine can be achieved at a very low level of fuel consumption. Hence, they reported that the only limitation to this approach is operating at stoichiometric conditions due to the risk of backfire and pre-ignition [8]. Improvements have been reported in thermal efficiency and indicated mean effective pressure (IMEP) of up to 38.9% and 14.2%, respectively, by increasing the density with relatively low NOx emissions [9]. The effect of supercharging hydrogen engines to improve performance and reduce NOx emissions are supported by other studies [10–14].

The performance of the hydrogen SI engine is enhanced by boosting the intake air pressure, but this increases the in-cylinder temperature which strongly influences the NOx formation rate [15]. The reduction of NOx emissions can be achieved by increasing the air–fuel ratio (lean burn) or by recirculating the exhaust gases (EGR). But, to enhance maximum thermal efficiency $> 40\%$, reducing heat loss is essential. The effect of lean burn on decreasing cooling heat losses is greater than that of EGR [16], so higher thermal efficiency and lower emissions are expected [17–21]. Lean burn of an SI engine occurs when the relative air/fuel ratio (AFR) is greater than unity. Moreover, high laminar flame speed of hydrogen can be used to offset the slow burning tendencies of the lean burn mixtures, offering greater combustion speed and stability [21].

* Corresponding author.
E-mail address: Colin.Axon@brunel.ac.uk (C.J. Axon).

https://doi.org/10.1016/j.fuel.2023.129192
Received 15 February 2023; Received in revised form 28 June 2023; Accepted 7 July 2023
Available online 14 July 2023

Nomenclature

a, m	Wiebe efficiency and form factors
m	mass (kg)
N	engine speed (rpm)
P	in-cylinder pressure (kPa)
Q	heat transfer (J/degree)
T	in-cylinder temperature (K)
U	internal energy (J)
V	volume (m^3)
W	work (J)
x	Wiebe mass fraction burned
α	mixture strength-dependant constants
β	mixture strength-dependant constants
θ	crank angle (degree)
∅	equivalence ratio
η	efficiency
γ	specific heat ratio
τ	autoignition delay
λ	excess air ratio
ε	standard error (%)

Acronyms

AFR	air/fuel ratio
aTDC	after top dead centre
bTDC	before top dead centre
CA	crank angle
CA50	location of 50% mass fraction burned
CI	compression ignition
CO_2	carbon dioxide
CR	compression ratio
ISFC	indicated specific fuel consumption (kg/kWh)
KI	knock integral
MAP	manifold air pressure (kPa)
MFB10-90	10–90% mass fraction burned
MFB50	50% mass fraction burned
NO	nitric oxide
NOx	oxides of nitrogen
RON	research octane number
ISFC	indicated specific fuel consumption (kg/kWh)
SI	spark ignition
SL	laminar speed (m/s)
ST	spark timing
TDC	top dead centre

Subscripts

0	initial condition
b	burnt mass
d	displaced volume
f	fuel
loss	heat losses
soc	start of combustion
u	unburnt mass

Table 1
Physico-chemical properties of hydrogen and gasoline.

Physico-chemical property	Hydrogen	Gasoline
Laminar flame speed at stoichiometric operation (cm/s)	185	40
Diffusion coefficient (cm^2/s)	0.61	0.16
Lean limit	0.1	0.5–0.6
Research Octane Number	>130	95–100

When the SI engine is operating at boosted lean conditions the dilution of air mixture will significantly increase, affecting the combustion stability, which can lead to autoignition, misfire or knock [22]. In studying the hydrogen combustion instabilities with a very lean mixture ($\lambda = 2.8$) for a part-load operation with a low engine speed, Nguyen et al. [20] showed that combustion remained stable without any backfire, misfire or knock. Lee et al. [23] demonstrated that the knock presence from the boosting pressure has an opposite relationship with the equivalence ratio due to the drop of the gas temperature, but knock did not occur once the mixture became leaner than the equivalence ratio of 0.6. By increasing boosted pressure, the lean burn limit increased up to equivalence ratio of 0.2, whereupon the thermal efficiency could be increased up to 36.7%. Studies of the knock-free regimes for a hydrogen-fuelled engine at various excess air ratios, compression ratios and load provide evidence to justify the selected operating condition to avoid combustion abnormalities [23–27]. Furthermore, hydrogen-fuelled SI engine knock can also be estimated in the same way as the existing gasoline knock models by using the appropriate modifications [26]. The aim of the knock model is to determine whether the engine knocks at a certain operating condition or not. The most commonly used method describes knock occurrence as a function of the autoignition delay [28].

Following the spark discharge, it is assumed that flame propagation produces a spherical growing flame with a speed close to laminar flame speed [29]. Then the laminar burning velocity correlation is used to estimate the influence of the equivalence ratio, initial pressure, temperature and residual gas content upon the total burn duration of hydrogen-fuelled SI engines at various speed and compression ratios [30]. The mass fraction of burned gases at any instant of the combustion process is specified using the Wiebe function [31]. For optimal performance the MFB50 location can be fixed at 8 °CA aTDC [32]. The specific heat ratio is replaced by a polytropic index appropriate for hydrogen–air mixtures [33]. Global models are preferred due to their simplicity and, when appropriately modified they produce outcomes that are comparable to those obtained using more precise models, such as multi-dimensional thermodynamic models.

Currently there are no single-zone studies correlating equivalence ratio, spark timing, compression ratio and intake pressure to investigate the combustion characteristics, NO emissions and knocking regions of a hydrogen-fuelled SI engine. In this study, the effect of boosted lean burn mixtures at various spark timings with pure hydrogen SI engines is investigated, and in-cylinder pressure, heat release rate, combustion duration, indicated thermal efficiency, indicated specific fuel consumption, NO formation rate and knock regions at various engine operating conditions are addressed.

2. Methodology for modifying the single-zone model

In comparison with complex 3D computational fluid dynamics studies, global models are simple, but if treated appropriately will yield comparable results. The starting point is the single-zone thermodynamic model [34]. This will be extended by implementing a laminar flame speed sub-model to determine the combustion duration, which will be incorporated in the Wiebe function to study the heat release rate and combustion performance under various operating conditions. The extended Zeldovich mechanism will be built into the single-zone model to calculate NO emissions, and finally the operating conditions that lead to knock will be obtained through the Livengood-Wu integral model.

2.1. Laminar flame speed sub-model

The single-zone model is modified by incorporating laminar flame speed to predict the combustion duration with respect to the reference operating conditions by using the inverse relative change in the laminar flame speed [30]; detailed in the Appendix A. Where the total combustion duration ($\Delta\theta$) is linear with burn duration ($\Delta\theta_0$) then,

$$\Delta\theta = \Delta\theta_0 \frac{g_{SL}}{g_{SL,0}} \tag{1}$$

where the function g incorporates the influence of laminar flame speed on burn duration. The determined combustion duration for each operating case is used in the Wiebe function (Eq. (2)) giving the gross energy released by the hydrogen-air mixture as a function of crank angle,

$$x_b = 1 - \exp\left[- a\left(\frac{\theta - \theta_{soc}}{\Delta\theta}\right)^{m+1} \right] \tag{2}$$

where θ is the instantaneous crank angle, θ_{soc} is start-of-combustion crank angle, a (set at 6.9) and m are efficiency and form factors, respectively, and $\Delta\theta$ is combustion duration (Eq. (1)). The experimental data for the combustion duration and shape factor m is fitted using the least-square method. The maximum error between the experimental and simulated value of m at various operating conditions was found to be 12% ($R^2 = 0.895$).

A correlation of laminar flame speed for hydrogen-air mixture as a function of equivalence ratio, pressure and temperature [35] is:

$$S_L = S_{L,0}(\varnothing)\left(\frac{T_u}{T_o}\right)^{\alpha}\left(\frac{P}{P_o}\right)^{\beta} \tag{3}$$

where $S_{L,0}$ is the laminar flame speed measured at ambient conditions at a given equivalence ratio $\varnothing$ when T_u corresponds to ambient temperature T_o and P corresponds to ambient pressure P_o, and α and β are mixture strength-dependant constants (see Appendix A). Moreover, P and T_u are pressure and temperature at the start of the combustion for each operating condition and obtained using the polytropic relation. The effect of residual gases on the laminar flame speed is not considered since it did not vary the ratio in Eq.1. Due to the flammability limits of hydrogen, the computation of laminar flame speed is performed for a wide range of equivalence ratios to validate the model against the available experimental studies [37–43]. However, few studies are available at the relevant conditions [41–43]. The derived analytical correlations of hydrogen laminar flame speed at elevated temperatures and pressures for equivalence ratios are shown in Table 2, and are easily implemented into spark ignition engine simulations [44].

Comparing the experimental data of laminar flame speed [36–39] with predictive calculation using the correlations of [40,42,43], the laminar burning velocity show a similar behaviour for a range of equivalence ratio from 0.5 to 3.0, with peak burning velocities located in the rich region from 1.4 to 2.0 with magnitudes between 2.5 and 3.0 m/s (Fig. 1). The computational flame speed curve accurately predicts the experimental data in the lean burn region, but the maximum flame velocity is underestimated with respect to the data of Pareja et al. [37].

Table 2
Hydrogen laminar flame speed correlations from various studies.

Reference	Pressure (MPa)	Temperature (K)	Equivalence Ratio (-)
Verhelst [40]	0.1–1.0	300–430	0.30–1.00
Verhelst et al. [41]	0.5–4.5	500–900	0.33–5.00
Ravi and Petersen [42]	0.1–3.0	270–620	0.50–5.00
Gerke et al. [43]			
Correlation 1	0.5–4.5	350–700	0.36–2.50
Correlation 2	0.1–8.0	300–900	0.40–3.75

Thermo-diffusivity and hydrodynamic instabilities are likely to be prevalent under engine operating conditions and can modulate the flame speed [36]. Thus, the computed flame speed might underpredict the burning velocity at elevated pressures. Nevertheless, the burning velocity of different mixture compositions will only be used to calculate the change of combustion characteristics at various equivalence ratio, spark timing, and intake pressure, hence it does not represent the laminar flame propagation nor the turbulent burning velocity. However, there is a trade-off between ease of use and the level of complexity of a model, and incorporating laminar flame speed is a useful addition to the single-zone model. Fig. 2 shows that the for the equivalence ratio range, the correlations of [41] and [43] are most useful due to extended lean burn limits at wider ranges of pressures and temperatures. The laminar flame speed correlation [43] can be incorporated in spark ignition engine simulation and the correlation provided acceptable results [44].

2.2. Heat release rate

From the first law of thermodynamics, the heat release is given by:

$$dQ_{ch} = dU + dW + dQ_{loss} \tag{4}$$

where the change of energy during combustion equals the change of the internal energy and the work done by the system. The derived heat release rate accounting for heat loss was modelled as:

$$\frac{dQ}{d\theta} = \frac{\gamma}{\gamma - 1} p \frac{dV}{d\theta} + \frac{1}{\gamma - 1} V \frac{dp}{d\theta} - dQ_{loss} \tag{5}$$

where γ is the specific heat ratio of the mixture, p is the in-cylinder pressure, and V is the instantaneous volume and dQ_{loss} is the convective heat loss modelled using Woschni correlation [45]. The heat transfer coefficient in the standard Woschni correlation is multiplied by a factor of 2.2 as proposed by [46] to match with the heat losses due to using hydrogen because of the low quenching distance of hydrogen and the high burning velocity resulting in greater cooling loses. The error of peak heat release is within 14% compared to the error of 57% when the standard Woschni correlation is used. For hydrogen, the constant specific heat ratio is replaced by a temperature dependent polytropic index accounting for hydrogen-air mixtures [33].

2.3. Engine simulation conditions

The initial and boundary conditions for the numerical model are directly related to the experimental data of a single cylinder four stroke hydrogen SI engine [18]. The values for boosted intake pressure, equivalence ratio and spark timing on the combustion and emission characteristics are given in Table 3. All the simulations were carried at a fixed compression ratio of 11.5 at an engine speed of 2000 rpm.

2.4. Evaluation of ICE performance

The indicated mean effective pressure (IMEP) is calculated using the in-cylinder pressure:

$$IMEP = \frac{1}{V_d}\int_{-360}^{+360} pdV \tag{6}$$

The indicated thermal efficiency is determined by calculating the ratio of the indicated power produced by the engine to the energy supplied by fuel per second:

$$\eta_{th} = \frac{Power}{m_f c_v} \tag{7}$$

The indicated specific fuel consumption is defined as the amount of fuel consumed by the engine per cycle.

$$ISFC = \frac{m_f}{Power} \tag{8}$$

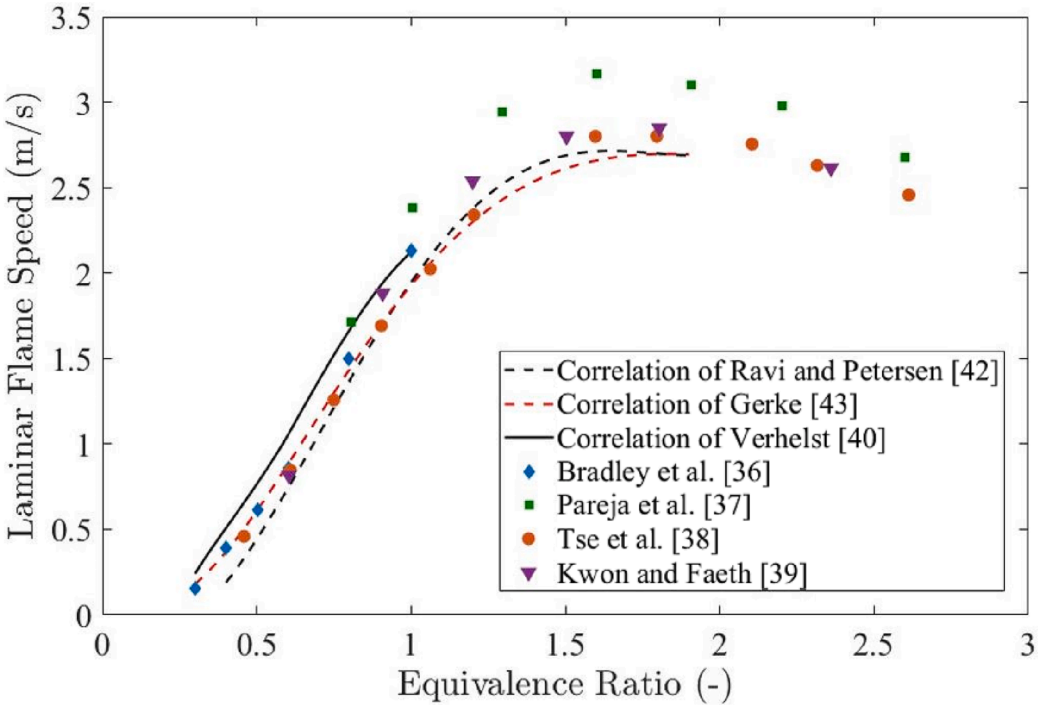

Fig. 1. Hydrogen-air mixture laminar burning velocity as a function of equivalence ratio at engine-relevant conditions ($T_0 = 300$ K, $P_0 = 1$ atm). Experimental values [36–39] are presented as symbols, computational results are presented as lines (Correlation 2 is used from [43]).

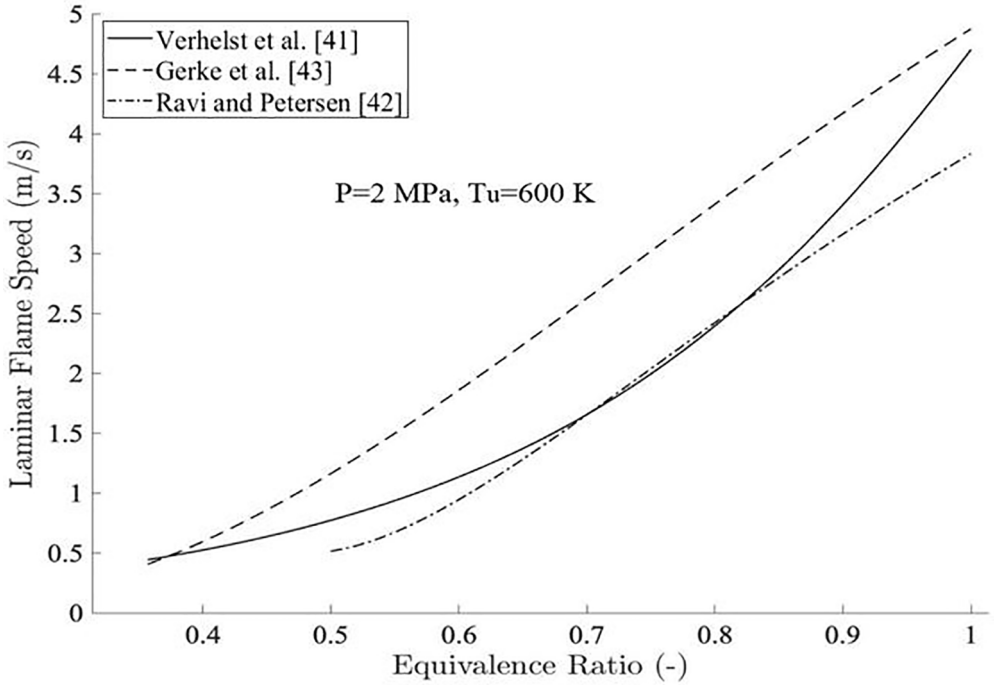

Fig. 2. Laminar flame speed of hydrogen at engine-relevant conditions for equivalence ratio at $P_0 = 0.5$ MPa, $T_0 = 350$ K (Correlation 1 is used from [43]).

Table 3
Operating conditions used for the simulations. Data sources: [17–19,47].

Parameters	Values
Spark Timing (°CA bTDC)	30 to 0
Equivalence ratio (-)	0.385 to 0.770
MAP (kPa)	84 to 134

2.5. NO emissions

Nitric oxides (NOx) are an exhaust emission requiring control in hydrogen-fuelled engines. The formation of NOx is dependent on in-cylinder temperatures (>1800 K), oxygen concentration, and reaction duration. Of the possible NOx emissions, nitric oxide (NO) is the main emission released [48]. The NO concentration was computed by integrating the chemical rate equations of the extended Zeldovich

mechanism [48].

2.6. Knock sub-model

Knocking is the main factor limiting the thermal efficiency of SI engines, and is related to charge density, compression ratio, and early spark timing [31]. It is defined as the auto-ignition of unburned mixture at the end-gas when temperature and pressure are high and governed by the time available for a reactive mixture to cover the auto-ignition delay time. Auto-ignition chemistry leading to the onset of knock, τ_{knock}, is determined by integrating the inverse of the ignition delay time,τ [28]. Knock occurs when the value of knock integral, *KI*, reaches unity,

$$KI = \int_0^{\tau_{knock}} \frac{dt}{\tau} \tag{9}$$

Since an Arrhenius correlation for hydrogen combustion was not available for varying equivalence ratios, the autoignition delay time for a hydrogen-air mixture was simulated in Chemkin [49]. for a range of temperature, pressure and equivalence ratios in a closed homogeneous reactor. A detailed multi-step chemical kinetic model of hydrogen-air combustion as proposed in [50] was used. The effect of ambient pressure on the autoignition delay time was not very significant therefore a representative averaged pressure was selected for an operating condition. The simulated data of autoignition time at different temperature was fitted using a least square algorithm to obtain an expression for each equivalence ratio considered. The unburned temperatures and pressures that are relevant to engine operating conditions were then used in the best-fit expression to determine the autoignition time and the knock integral. The temperature of unburned gas T_u [51] is,

$$T_u(\theta) = T_{u,soc}\left(\frac{p(\theta)}{p_{soc}}\right)^{\frac{\gamma-1}{\gamma}} \tag{10}$$

where the specific heat ratio is replaced by the polytropic index accounting for hydrogen-air mixture [33]. Hydrogen-fuelled engines are vulnerable to pre-ignition which can lead to knock [25]. The proposed knock model only captures the autoignition of the unburned mixture at the end-gas. The presence of hot spots or emissions from unburned hydrogen of the previous cycle can also cause pre-ignition [27]. In this study the pre-ignition was not considered since the hot spots could not be identified for a single-zone model.

3. Results and discussion

The modified single zone thermodynamic model with the incorporation of laminar flame speed sub-model, NO emission sub-model, and knock intensity prediction sub-model were used to study the NO emissions from a hydrogen fuelled SI engine under boosted and lean burn operating conditions. The combustion performance was investigated under the engine operating conditions (Table 3) by analysing in-cylinder pressure, temperature, heat release rate, and combustion duration. The prediction of the NO emissions and knocking region was also examined.

3.1. Model validation

The simulation results for in-cylinder pressure and heat release rate at different equivalence ratios, spark timings and engine speeds were validated using published experimental data [18], the corresponding specifications of their single cylinder engine are given in Table 4. The effects of lean burn operation and intake air pressure boosting on engine performance was validated with the study of Gürbüz and Akçay [9].

Table 4
SI engine specifications used in simulations.

Characteristic	Sementa et al. [18]	Gürbüz and Akçay [9]
Bore × Stroke [mm]	72 × 60	85.7 × 82.6
Displacement Volume [cm^3]	244.3	476.5
Speed [rpm]	2000	1600
Compression Ratio [-]	11.5	8

The in-cylinder pressure data was selected to assess the effectiveness and reliability of the numerical model, Fig. 3 presents the experimental and numerical results for the in-cylinder pressure and heat release rate variations at two lean operating conditions ($\lambda = 1.30$ and $\lambda = 2.00$) at 2000 rpm and compression ratio of 11.5. The model predictions were satisfactory during the compression and expansion processes, but a difference of $>2\sigma$ was observed during the combustion process. The simulated in-cylinder combustion pressure profile was under-predicted due to the lack of detailed chemical reaction mechanisms, assuming that the burning velocity is laminar, and not accounting for the effect of thermal diffusivity and pressure attributed to Darrieu-Landau instabilities [36]. The quantitative variation between the experimental data and model results were evaluated, and the standard error (ε) was found to be 3% for $\lambda = 1.30$ and $\lambda = 2.00$ condition with a maximum deviation value d_{max} of 142 kPa. Moreover, the heat release rate for both lean operating conditions at $\lambda = 1.30$ and $\lambda = 2.00$ was predicted satisfactorily by the current model which also accounts for heat loss (Eq. (5)).

Fig. 4 shows the validation of simulated indicated mean effective pressure and maximum in-cylinder pressure at various spark timings from 30 bTDC to TDC for different intake pressures. The simulation results were compared with the experimental work of Gürbüz and Akçay [9]. The maximum error of the simulated results was 3%, which is within the cycle-to-cycle variation of the experimental conditions.

3.2. Combustion performance

The operation of naturally aspirated hydrogen IC engines under lean mixture conditions could lead to performance reduction, therefore it is beneficial to boost the manifold air pressure to achieve power comparable to existing gasoline engines [8]. The boost pressure supplied to the engine either by a supercharger or turbocharger at the inlet is further amplified during compression, which is a function of the compression ratio and temperature. The application of increased intake air pressure affects the combustion characteristics. Fig. 5 shows the variation of the simulated in-cylinder pressure traces at different manifold air pressures (MAP = 84 kPa, MAP = 114 kPa, MAP = 134 kPa) and excess air ratios ($\lambda = 1.54$, $\lambda = 2.00$). The simulation does not account for the mechanical losses incurred by the charger. Increasing the intake air pressure affects the in-cylinder pressure, where the pressure at the end of compression changes from 1.39 MPa for a MAP of 84 kPa to 2.22 MPa for the MAP of 134 kPa at $\lambda = 1.54$ at 2000 rpm. This is mainly due to an increase in volumetric efficiency caused by an increase in the amount of air compressed at higher pressure, altering the combustion process, hence, for $\lambda = 1.54$ operation the peak in-cylinder pressure increased from 4.42 MPa to 57.52 MPa when the MAP was increased from 84 kPa to 134 kPa. The observed increase in combustion performance from increasing the intake air pressure for $\lambda = 1.54$ operation was not the same for leaner mixtures due to an increase in the amount of air inside the chamber. Operating conditions that correspond to mixtures leaner than $\lambda = 2.00$ result in a reduction in burning speeds, hence the spark timing had to be advanced to compensate for the longer combustion duration. The instantaneous heat release rate shows the characteristics of the combustion process. The heat release rate decreased significantly with much leaner mixtures due to the lower amount of the fuel in the mixture and slower combustion speed caused by the increase of air. Also note from the inset plot in Fig. 5 that the peak heat release rate shifted slightly with boosting pressure under $\lambda = 1.54$ operating condition. But under lean mixture operation ($\lambda = 2.00$) the peak heat release rate shifted significantly by 20 °CA from 360 °CA to 380 °CA, and the peak magnitude also decreased from 31 J/°CA to 15 J/°CA. The total amount of heat release increased with increasing boosting pressure at $\lambda = 1.54$ due to increased amount of fuel required to maintain constant λ. For leaner mixtures (λ =

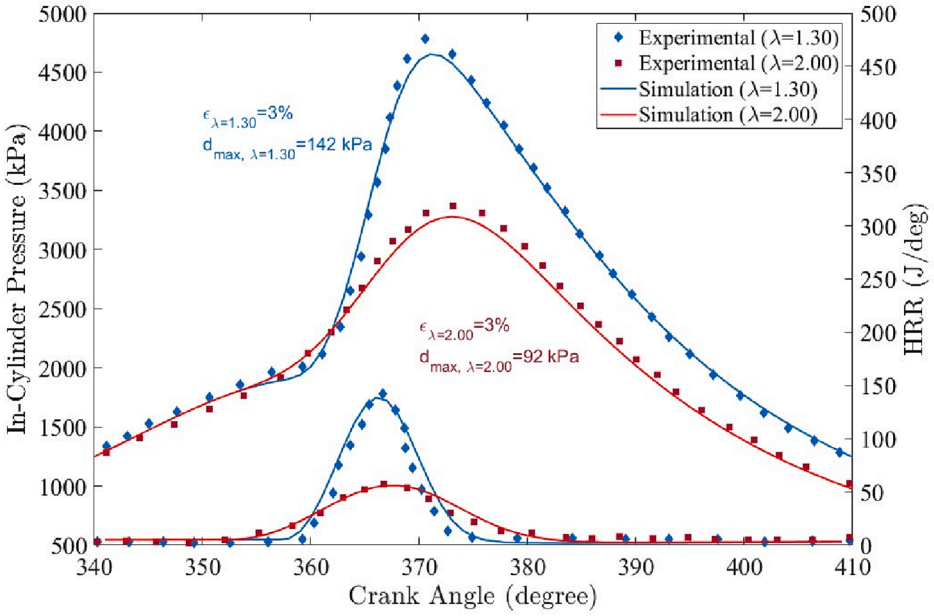

Fig. 3. In-cylinder pressure and heat release rate of hydrogen-air mixture, experimental values [18] are presented as symbols, computational results are presented as a solid line (MAP = 84 kPa, CR = 11, N = 2000 rpm, $ST_{\lambda=1.30}$=3 °CA bTDC, $ST_{\lambda=2.00}$=12 °CA bTDC).

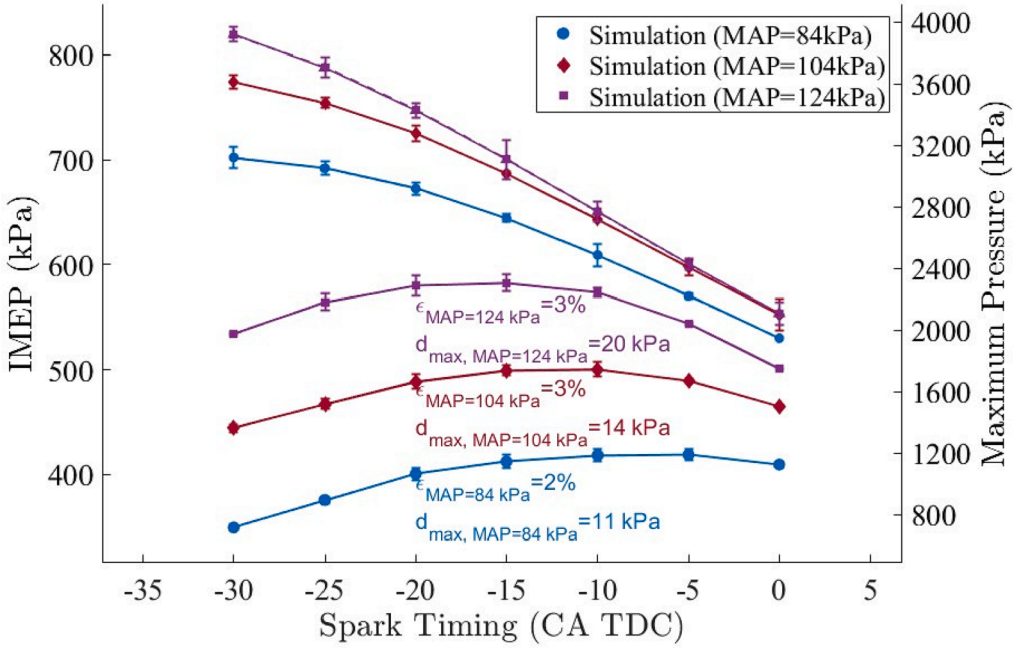

Fig. 4. Experimental and simulated results for indicated mean effective pressure and maximum in-cylinder pressure at equivalence ratio of 0.6. Experimental values [9] are presented with error bars, computational results are presented as a solid line (CR = 8.1, N = 1600 rpm).

2.00), the total magnitude of heat did not vary significantly with higher boost pressures. This was due to the reduction of in-cylinder pressure caused by the longer combustion duration due to increased amount of leaner mixture inside the chamber.

Fig. 6 shows the simulated peak in-cylinder pressure for various λ and MAP cases for MBT timing at 2000 rpm. The peak cylinder pressure increases linearly for $\lambda < 1.82$ because of the increasing amount of hydrogen in the fuel–air mixture. As the boost pressure increases, the energy supply increases, hence higher peak in-cylinder pressure values occurred at MAP of 134 kPa and $\lambda = 1.30$ with a magnitude of 7.14 MPa. Furthermore, for $\lambda > 1.82$, any increase in the intake air pressure results in lower peak cylinder pressure due to lower burning speed caused by air dilution and by the reduced amount of the hydrogen in the mixture. The simulated peak cylinder pressure of 7.14 MPa for the hydrogen engine did not exceed the values found for a gasoline fuelled SI engine under the same operating conditions [52]. The maximum peak pressure rise can be controlled by adjusting the spark timing, but the data correspond to MBT timing for each operating condition.

3.3. Mass fraction burn and knocking regime

The mass fraction of fuel burnt (MFB) and the location of end-gas autoignition are required to determine the knocking intensity i.e. instantaneous mass fraction burned per crank angle for each operating

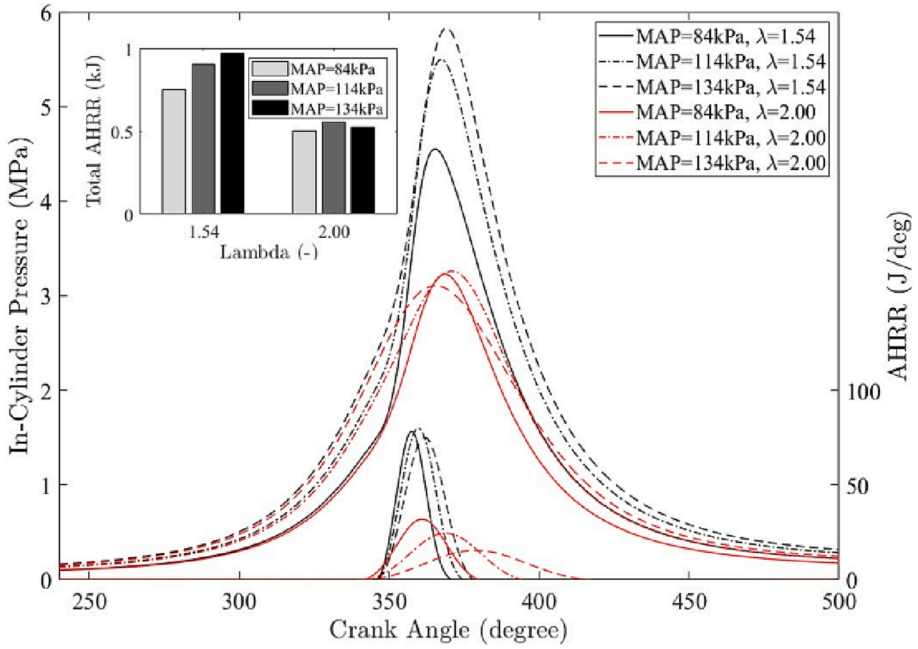

Fig. 5. Results for in-cylinder pressure and AHRR curves with boosting pressures of 84 kPa, 114 kPa and 134 kPa and excess air variation (λ = 1.54, 2.00), to compare charging pressure effect at different lean conditions (CR = 11.5, N = 2000 rpm, ST = 10 °CA bTDC).

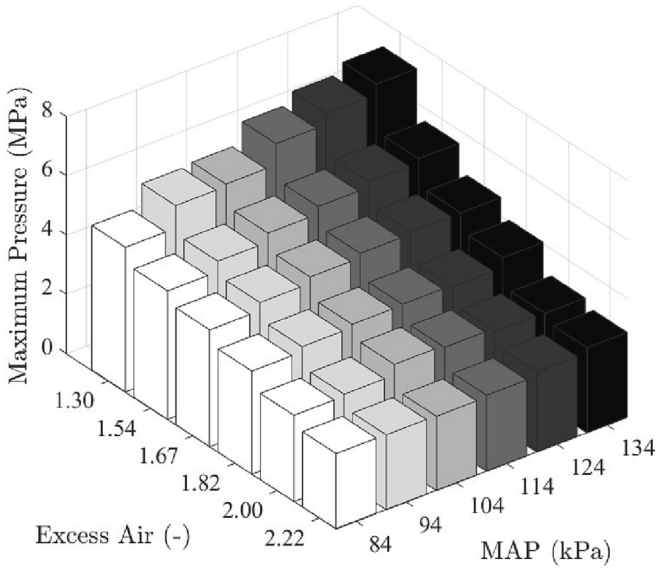

Fig. 6. Maximum in-cylinder pressure values for boosted pressures varying from 10 kPa to 50 kPa with 10 kPa increment at lean burn conditions from λ = 1.30 to λ = 2.22 (CR = 11.5, ST = MBT).

condition. Fig. 7 shows the mass fraction profile as a function of crank angle for each boosted condition for λ = 1.82 at a fixed spark timing of 15 °CA bTDC. The hydrogen-air mixture burns at a fast rate after the spark discharge and peaks around halfway through combustion, and then drops to near zero towards the end of combustion. Hence, the MFB period increases with increasing intake pressure due to the increased amount of hydrogen-air mixture [9]. As a result of added air intake pressure, the combustion duration is prolonged, increasing knocking tendency [53]. Since combustion duration was found to be a good indicator of knock occurrence, it is reasonable to use the mass fraction burned curves to characterise the combustion stages by their duration in terms of crank angles. Combustion duration (CA10-90) is the crank angle interval required to burn the bulk of the mixture, which is defined as the time between the start of flame development (10% mass fraction burned) and the end of flame propagation (90% mass fraction burned). Fig. 8 (a) shows the combustion duration of the hydrogen-air mixture under varying MAP and λ. A leaner mixture results in an increase in CA10-90 due to slower burning velocity and increased flame development angle (CA0-10). This is caused by the slower laminar flame speed, due to the reducing equivalence ratio [31]. This means that CA10-90 is not only a factor affecting combustion efficiency, but the entire flame propagation depends on the flame kernel initiation process. In addition, the MAP has a greater impact on leaner mixture operation due to the increase of air volume. For a MAP of 134 kPa the combustion duration increases significantly up to 53 °CA when the mixture was leaner than λ = 2.22, and the combustion duration increased by 60% when MAP was increased from 104 kPa to 134 kPa. Also, the crank angle at which 50% of fuel burned (CA50) must be located between 8 and 10 °CA aTDC for optimum performance [32,34].

Fig. 8 (b) shows that CA50 shifts away from the optimal location when the mixture becomes leaner. For the naturally aspirated condition at a MAP of 84 kPa, the CA50 location shifts significantly away from optimal location for λ > 2.22. However, for higher boosted pressures the increase of CA50 occurs after λ = 2.00 for the MAP of 104 kPa and 114 kPa, and just after λ = 1.82 for the MAP of 134 kPa. This is mainly due to less fuel in the mixture, hence slower flame speed giving longer combustion durations. Therefore, the combustion location of CA50 could not be centred at 8–10 °CA after TDC. Furthermore, slower-burning mixtures require increased spark advance to achieve the optimal indicated thermal efficiency. Fig. 8 (c) shows how the load is affected by the CA50 point at different MAP values. The load increases as the CA50 is positioned at the optimal location around 8–10 °CA aTDC and reduces as the CA50 shifts away the optimal position.

Using the operating conditions in Table 3 with the Livengood-Wu knock model, Fig. 9 shows the knock integral for various manifold air pressures and equivalence ratios at MBT timing, 10 °CA retardation and advance from MBT timing. It can be seen that knock did not pass unity at MBT timing conditions. This is in agreement with previous work of [23], which showed that knocking did not occur for equivalence ratios lower than 0.6 (λ > 1.67) for hydrogen fuelled SI engines. However, knocking was observed when the spark timing was advanced where the knock integral exceeded unity for the MAP of 134 kPa and λ = 1.30. This

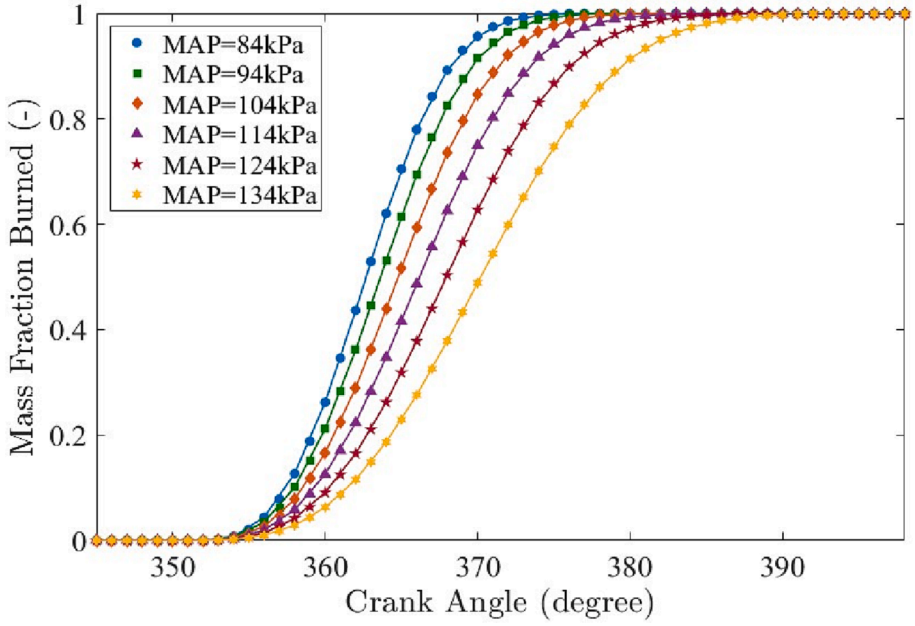

Fig. 7. Results for mass fraction burned profile for MAP as a function of crank angle at λ = 1.82 (CR = 11.5, N = 2000 rpm, ST = 15 °CA bTDC).

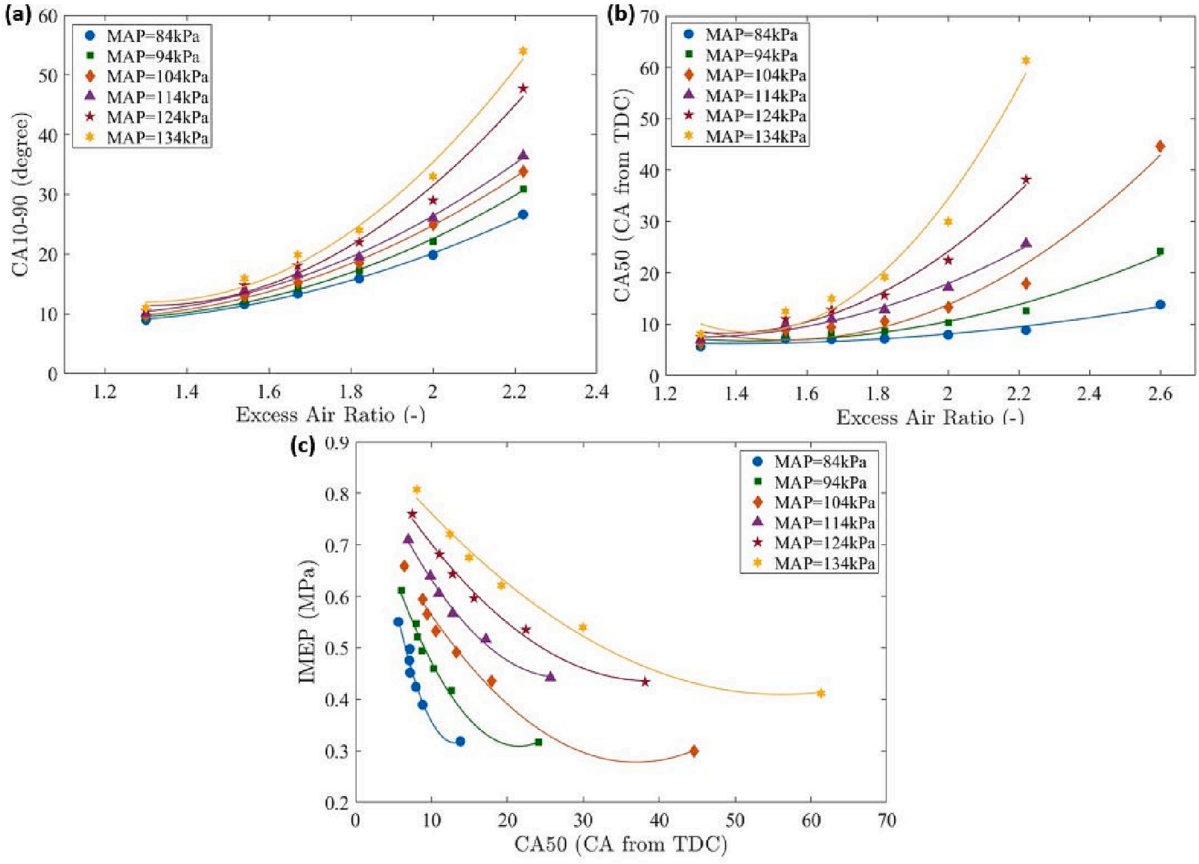

Fig. 8. Combustion duration CA10-90 (a), (b) location CA50 for various λ and MAP at MBT timing for each operating condition and (c) location of CA50 at different loads.

operating regime shows a tendency to knock due to the increasing charge density caused by the additional air inducted into the engine. Fig. 9 also shows a reduction in the tendency to knock when the spark timing was retarded, which could reduce the end-gas temperature and lengthen the auto-ignition delay time. However, retarding spark timing could lower thermal efficiency, hence knocking might prevent the engine from running with the optimal spark timing.

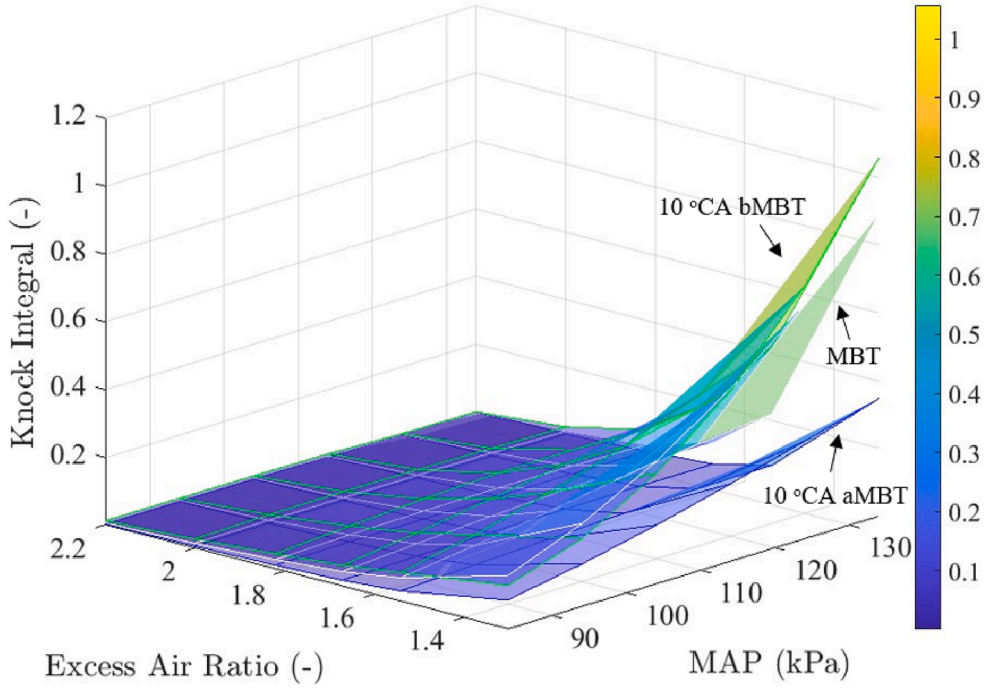

Fig. 9. Knock integral *KI* for different operating conditions and spark timings showing tendency of knock occurrence.

3.4. Impact of spark timing, λ and MAP on IMEP and ISFC

The optimal spark timing of the engine is mainly determined by the nature of the flame propagation within the combustion chamber, and the important parameters are: engine speed, engine load, engine temperature, intake temperature, fuel composition, and air excess ratio [31]. The spark timing is fixed at the minimum spark advance for best torque (MBT) location, and is evaluated as a function of equivalence ratio and boosting pressure to ensure maximum thermal efficiency under all operating conditions. Therefore, MBT timing for highest indicated mean effective pressure (IMEP) is determined by varying spark timing for $\lambda = 1.82$, and for boosting pressures varying between 84 kPa and 134 kPa (Fig. 10 (a)). For the naturally aspirated conditions of MAP up to 114 kPa the MBT timing was found to be at 15 °CA bTDC, then it increases to 20 °CA bTDC. With increasing intake air pressure, the minimum advance for best torque shifts away from TDC due to increasing charge density for higher manifold air pressures. For boosting pressures<114 kPa the MBT timing was not affected noticeably by increasing intake air pressure (advances < 2 °CA). As the intake pressure increases from 84 kPa to 114 kPa the peak value of IMEP initially increases by approximately 1.2 bar, thereafter the IMEP increases only marginally (by ≈ 0.7 bar). Thus, the power increase is explained by the additional charge inside the cylinder [54].

The MBT timing shifts from TDC when the charge became leaner (Fig. 10 (b)). At $\lambda = 1.30$ the MBT timing is at 10 °CA bTDC, but under ultra-lean conditions ($\lambda = 2.60$) is at 20 °CA bTDC. This is explained by the increasing combustion duration due to the decreasing burning velocity (less hydrogen in the mixture). The IMEP was reduced by operating under leaner mixtures due to lower burning speed. Fig. 10 (b) also shows that IMEP is reduced by up to 42% when the excess air ratio was doubled from $\lambda = 1.30$ to $\lambda = 2.60$ at their respective MBT timing under naturally aspirated operating conditions. The in-cylinder mixture composition λ was the most influential parameter on MBT timing, in line with previous work [47].

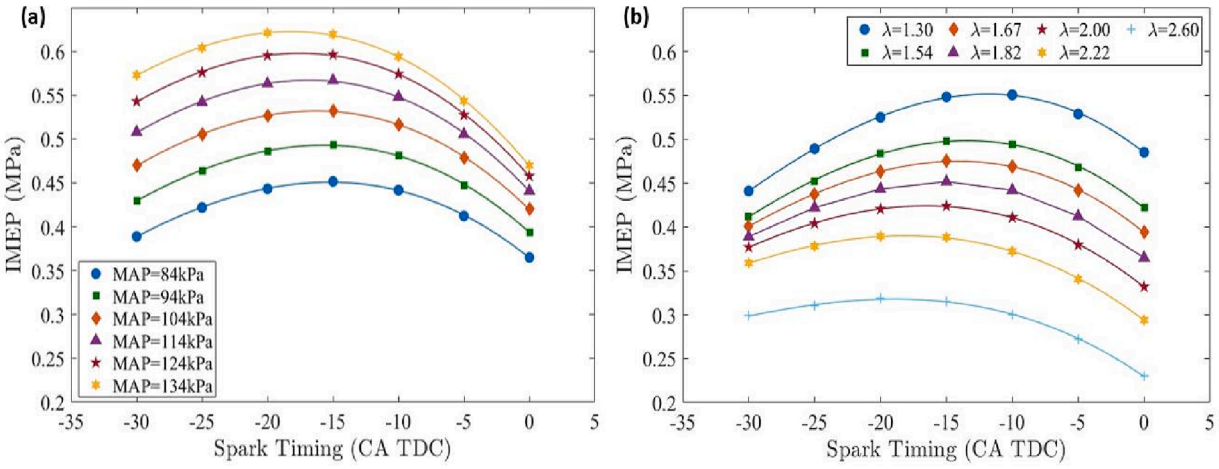

Fig. 10. Variation of IMEP (a) at various spark timing with MAP under $\lambda = 1.82$ and (b) at various spark timing at different λ for naturally aspirated condition (MAP = 84 kPa, CR = 11.5, N = 2000 rpm).

Fig. 11 shows the calculated IMEP with respect to λ and MAP at their respective MBT spark timing. The maximum IMEP (0.81 MPa) is reached for λ = 1.30 and MAP of 134 kPa due to increasing burning velocity. Operating under very lean conditions (λ > 2.22) the IMEP varied only by up to 6% when the charge was boosted (MAP = 84–134 kPa). Under relatively lower excess air-ratio operation (λ = 1.30) IMEP varied by up to 32% when MAP was boosted from 84 kPa to 134 kPa, but when operating at very lean conditions boosting had negligible effect on IMEP. This may be due to the reduction of the flame speed. Furthermore, increasing charging pressures had little effect on IMEP for mixtures leaner than λ = 2.00. To achieve higher loads comparable to a gasoline engine, the boosted hydrogen SI engine could be run at equivalence ratios closer to stoichiometric operation with exhaust gas recirculation to mitigate knock and reduce NO emissions [8].

3.5. Indicated thermal efficiency and indicated specific fuel consumption

Indicated thermal efficiency (ITE) shows how effectively the chemical energy of the fuel is converted into mechanical work (defined in Eq. (7). Fig. 12 shows the effect of λ and MAP on ITE, at the optimum spark timing for best torque at an engine speed of 2000 rpm. The ITE increases proportionally with boosted pressure reaching about 39% for λ = 1.82 at MAP of 84 kPa, whereas it reaches 42% with an increment of intake pressure by 40 kPa. For boosting pressures<94 kPa, ITE increases linearly with increasing λ. For naturally aspirated conditions (MAP = 84 kPa), ITE increases by approximately 21% with the excess air ratio increasing from λ = 1.30 to λ = 2.22. When the charging pressure increases beyond 114 kPa, the ITE peaks around λ = 1.82. This is in agreement with Luo et al. [55], where the highest thermal efficiency was achieved for equivalence ratios between 0.65 and 0.80 (λ = 1.53–1.25). Likewise, for mixtures leaner than λ = 2.22, boosting pressure did not increase ITE beyond boost pressure values of 94 kPa. The maximum simulated ITE – approximately 42% – occurs at λ = 1.82 at a MAP of 124 kPa. This study does not include the effect of unburned hydrogen emissions which might result in a reduction of ITE [56].

Indicated specific fuel consumption (ISFC) evaluates how effectively the thermal power of fuel is converted to indicated power. Fig. 13 (a) shows that under naturally aspirated condition of 84 kPa MAP, the ISFC was reduced by 17% when the engine operation was varied from λ = 1.30 to λ = 2.22. As per the boosting effect, ISFC reduced as MAP increased for the naturally aspirated condition at λ = 1.30. For MAP of 84 kPa, the ISFC increases as the mixture becomes leaner than λ = 2.22. Whereas for MAP of 114 kPa and 134 kPa the ISFC increases when mixture becomes leaner beyond λ = 2.00 and λ = 1.82, respectively. These findings correlate well within the shift of CA50 (Fig. 8 (b)), and agree with previous studies [55].

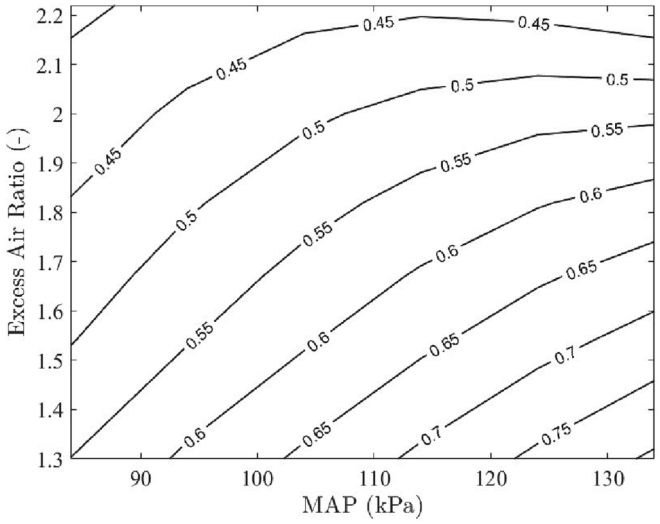

Fig. 11. Variation of IMEP (MPa) at various spark timing for different λ for naturally aspirated condition (MAP = 84 kPa, CR = 11.5, N = 2000 rpm).

Fig. 13 (b) depicts the spark timing effect on ISFC at various λ at naturally aspirated condition (MAP = 84 kPa). The optimal ISFC value occurs when the spark timing approaches MBT timing (the highest indicated power output). In general, the increase in manifold air pressure reduces the fuel consumption for mixtures with λ < 1.82 (Fig. 13 (c)). This reduction of fuel consumption results from the changes of the mixture composition. As MAP increases from 84 kPa to 94 kPa the ISFC decreases (except for λ = 2.60) where the load was found to decrease when the MAP was increased from 84 kPa to 94 kPa. The observation was due to a significant increase of the combustion duration caused by an increase of air dilution at boost pressures for lean burn mixtures (λ = 2.60). For λ = 1.30 and λ = 1.82 the ISFC reduces by 13% and 7% for increases of MAP from 84 kPa to 134 kPa, respectively.

3.6. Nitric oxide emissions

This section explores a strategy to reduce NO emissions of hydrogen engine by operating it under lean conditions. The simulated results of boost pressure (MAP) on NO emission at different λ are shown in Fig. 14 (a). Boosting the intake pressure increases the NO emissions and this effect was seen prominently when the engine was operated with λ < 2.00. The increase of NO emissions is explained by the in-cylinder temperature increase caused by supercharging, as the NO formation is dependent on high local temperature and excess oxygen. Operating beyond λ = 2.22, the NO emissions reduce for higher boosted pressures (MAP of 134 kPa) (Fig. 14 (a)). Because by increasing λ > 2.22 causes the temperature to decrease significantly, reducing NO formation to nearly zero and is in agreement with previous work [57]. Reductions of NO emissions occur with increasing λ for the corresponding MAP values (Fig. 14 (b)).

NO emissions are also reduced by retarding the spark timing with respect to MBT timing (Fig. 14 (c)), due mainly to reducing the global in-cylinder temperature. For an λ = 1.82 and MAP of 134 kPa, NO emission reduces by up to 68% when retarding the spark by 10 °CA (from 15 to 5 °CA bTDC). However, retarding the spark timing marginally reduces ITE (Fig. 14 (d)). For λ = 1.82 and MAP = 84 kPa, the NO emissions reduce by 55% and ITE reduces by 6% when spark timing is retarded by 5 °CA from MBT. Then when spark timing is retarded by 10 °CA the NO emissions almost drop to zero and the ITE reduces by 14%.

3.7. Summarising the operation of MAP in hydrogen SI engines

The model and simulations described can be drawn together to describe how the NO emissions from a hydrogen ICE can be controlled using the in-cylinder combustion processes. The IMEP and NO emission reduce while ITE increases (Fig. 15 (a)), with ITE peaking at around 42% for an absolute intake pressure of 124 kPa at λ = 1.82. By increasing the intake manifold air pressure further than 124 kPa the engine operates at higher loads, but the ITE reduces because the CA50 combustion location cannot be centred on 8 °CA aTDC due to the retardation of spark timing to mitigate knock. The IMEP and NO emission variation with spark timing (for λ = 1.82, Fig. 15 (b)), shows that the highest ITE is achieved at the MBT timing for each operating condition due to the highest power output. ITE and load varies proportionally with spark timing, hence the NO emissions can be reduced by retarding spark timing at a slightly reduced IMEP. This also mitigates knock (Fig. 9). Fig. 15 (a) also shows that the reduction of NO emissions was more pronounced by varying the mixture composition, as it influences the in-cylinder temperature and inhibits the NO formation process to almost zero level under ultra-lean burn operation of SI hydrogen engine.

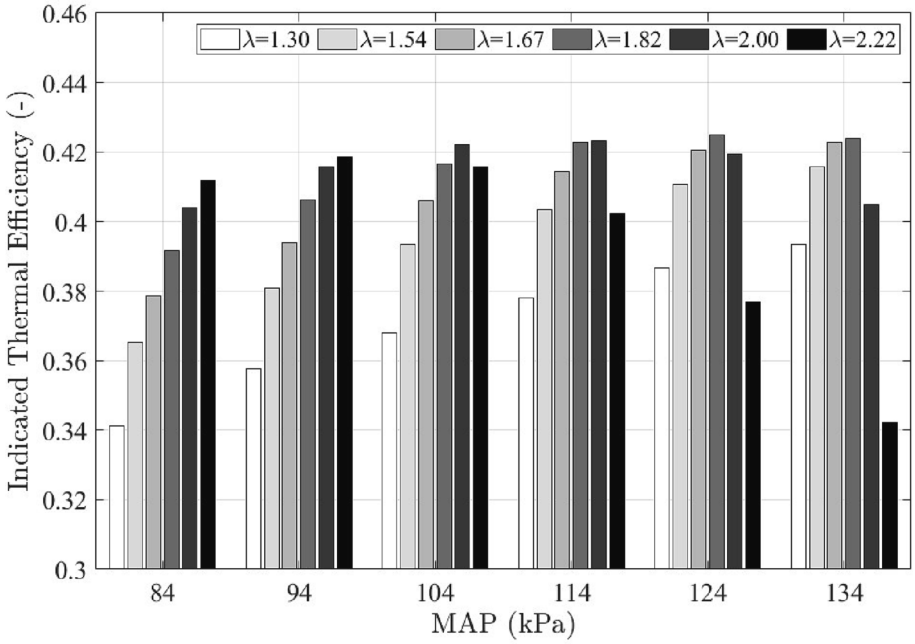

Fig. 12. Indicated thermal efficiency at various MAP (84–134 kPa) and lean conditions (λ = 1.30–2.22), to estimate optimal efficiency for different operating conditions (CR = 11.5, N = 2000 rpm).

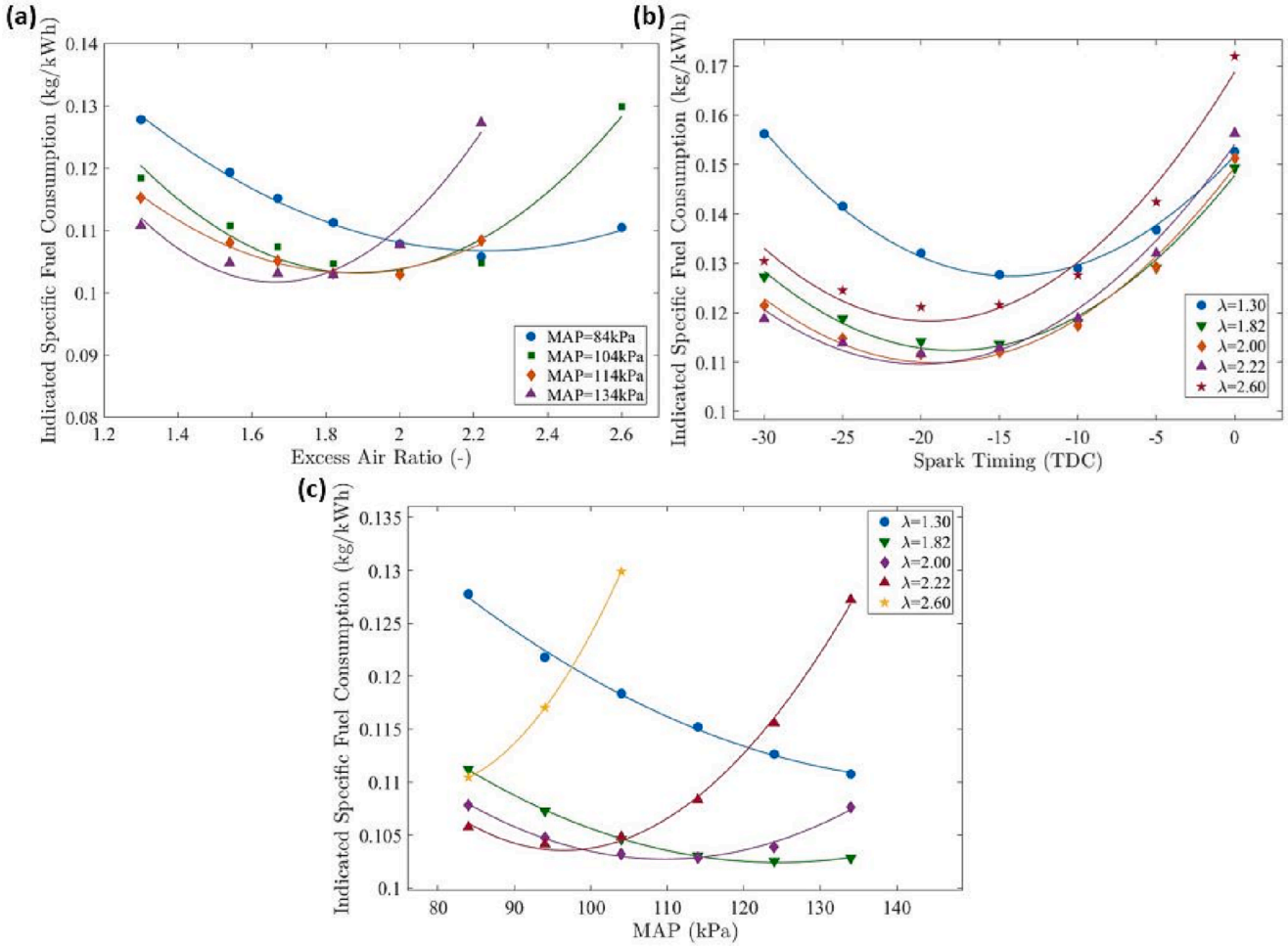

Fig. 13. ISFC values (a) at different λ and MAP at MBT timing, (b) at different λ and spark timing MAP = 84 kPa) and (c) at λ ratio and MAP at MBT timing.

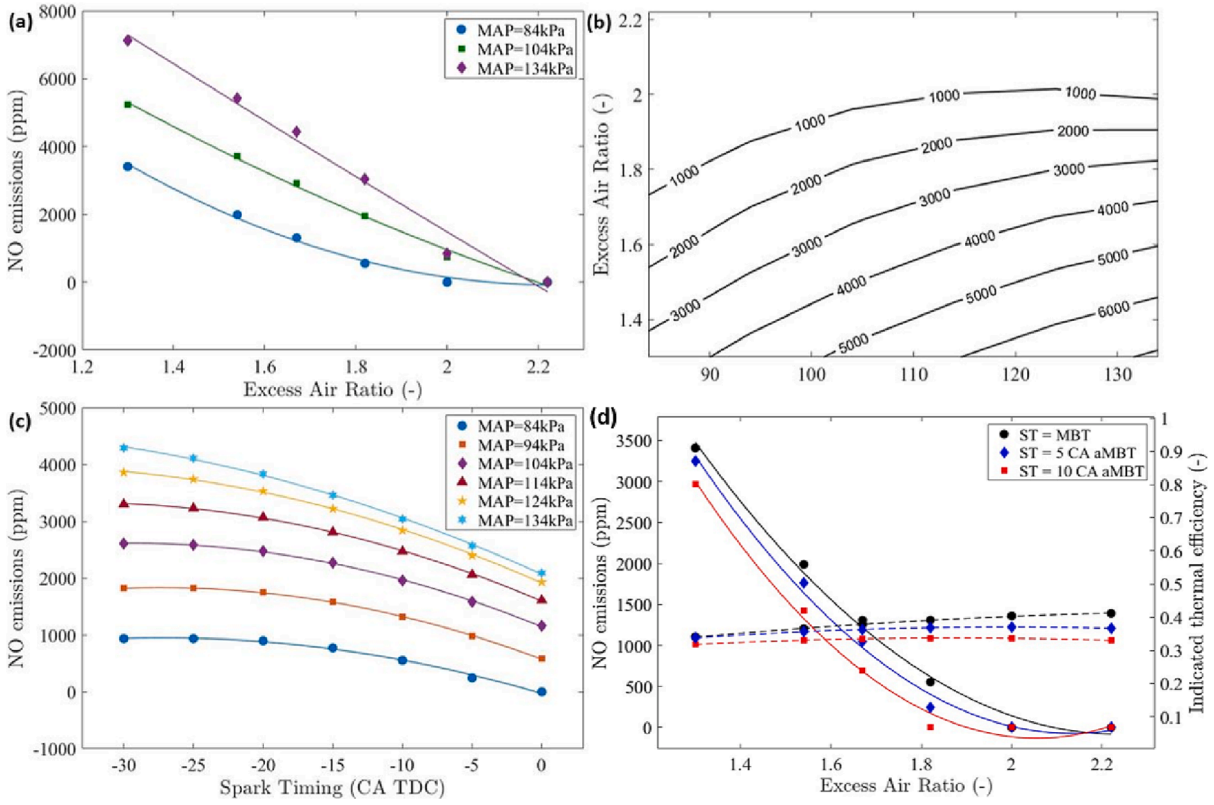

Fig. 14. NO emissions (a) at various λ and MAP at MBT timing, (b) NO emissions at various λ and MAP at MBT timing, (c) NO emissions at λ = 1.82 and at different spark timing and MAP and (d) NO emissions and indicated thermal efficiency at different λ operating at MAP of 84 kPa (naturally aspirated) at different spark timing of MBT, 5 °CA and 10 °CA retardment with respect to MBT timing.

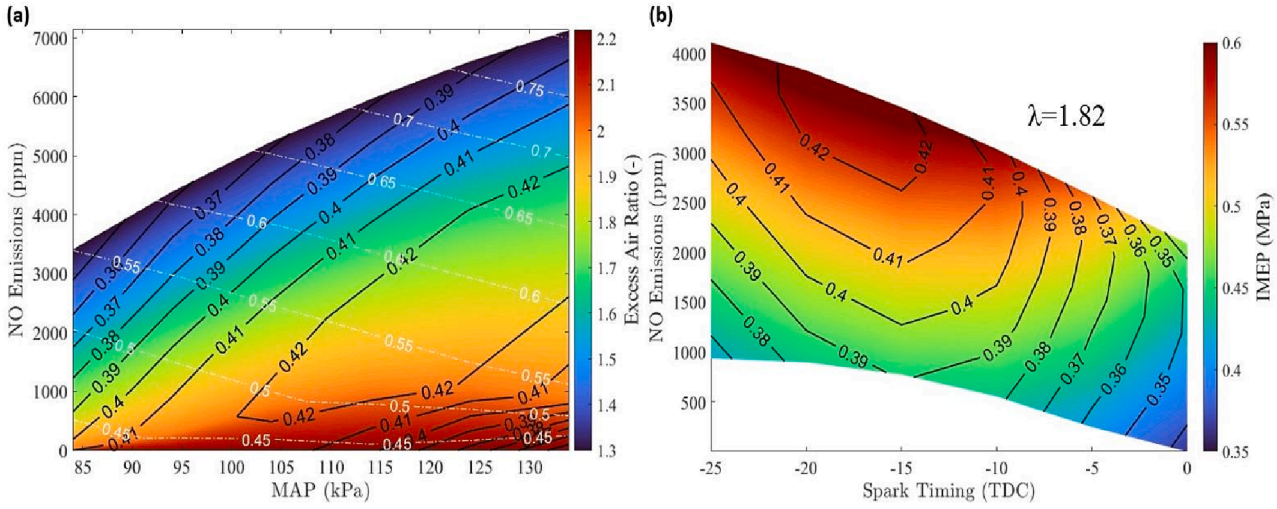

Fig. 15. Plots for the operation of hydrogen SI engines to control NO emissions: a) MAP, λ, and the knock region; b) IMEP and spark timings at λ = 1.82. ITE is shown as a heat map and contour lines, whilst the dashed white line represents IMEP.

4. Conclusion

Extending the single-zone thermodynamic model for SI engines to boosted lean burn hydrogen provides a useful tool for investigating this future low-carbon fuel. Furthermore, it gives insight into the potential gains in ITE which may be possible. The novel improvements are implemented using a laminar flame speed sub-mode to investigation the combustion, and NO emission and knocking characteristics of boosted lean burn combustion. The simulated cylinder pressure, heat release rate, and peak cylinder pressure are validated with experimental results, agreeing to within the standard error of cycle to cycle fluctuations. The simulations show that a naturally aspirated hydrogen-fuelled SI engine can operate λ = 1.30 to λ = 2.60. However, CA50 could not be centred at the optimal position for mixtures operating leaner than an λ = 2.22, particularly when the boost pressure exceeds 114 kPa. This is because high dilution leads to a longer combustion duration. The simulations indicated that boosted lean-burn operation improves the ITE up to 42% (at λ = 1.82 under manifold air pressure of 124 kPa at a load of 6 bar

IMEP). Once validated, the NO emissions model shows that emissions increase with boost pressure; but optimizing the start of combustion and the excess air ratio curtails this increase. For an $\lambda = 1.82$ the NO emissions reduce by 55%, almost dropping to zero, but reducing ITE only marginally. Further experimental work is required to substantiate the proposed boosted lean-burn hydrogen SI engine technology.

CRediT authorship contribution statement

D.N. Rrustemi: Formal analysis, Investigation, Methodology, Software, Validation, Visualization, Writing – original draft. **L.C. Ganippa:** Methodology, Supervision, Writing – review & editing. **C.J. Axon:** Conceptualization, Project administration, Supervision, Writing – review & editing.

Declaration of Competing Interest

The authors declare that they have no known competing financial interests or personal relationships that could have appeared to influence the work reported in this paper.

Data availability

Data will be made available on request.

Appendix A. Calculating the combustion duration

Lindström et al. [30] show that the burn duration varies inversely with equivalence ratio. The value of laminar flame speed does not represent the flame propagation, it is only used to find the relative the total combustion duration:

$$\Delta\widehat{\theta}_{SL} = \Delta\theta_0 \frac{g_{SL}}{g_{SL,0}}$$

Taking experimental values [9], $\Delta\theta_0$ is initially set to be 30 °CA for $\varnothing = 0.6$ and MAP of 84 kPa. After finding the combustion duration at one operating condition. Additional values at different equivalence ratios are found by using the laminar flame speed correlation of Gerke et al. [43]. The Gerke et al. correlation is valid at $0.1 \leq P \leq 4.5$ MPa, $350 \leq Tu \leq 700$ K, $0.36 \leqslant \Phi \leq 2.50$ ($P_0 = 20$ atm, $T_0 = 600$ K):

$$u_l = u_{l0}\left(\frac{T_u}{T_0}\right)^{\alpha}\left(\frac{P}{P_0}\right)^{\beta}$$

$$u_{l0} = \begin{cases} 0.25\Phi^6 - 3.4774\Phi^5 + 18.498\Phi^4 - 46.525\Phi^3 + 52.317\Phi^2 - 13.976\Phi + 1.2994, & 0.4 \leqslant \Phi \leqslant 2.5 \\ u_{l0}(\Phi = 2.5) + [7.23 - u_{l0}(\Phi = 2.5)]\dfrac{\Phi - 2.5}{2.5}, & \Phi > 2.5 \end{cases}$$

$$\alpha = 0.0163\left(\frac{1}{\Phi}\right) + 2.2937$$

$$\beta = 0.2037\left(\frac{1}{\Phi}\right) - 0.575$$

The variation of total combustion duration with engine speed is only used for one instance to match the simulated combustion duration with experimental data. This is valid because the engine speed is kept constant for this simulation. The spark timing effect on the total combustion duration is captured by the laminar flame speed, p_{ST} and T_{ST} which were taken at spark timing for all cases. A correlation for the ignition delay time is not considered since the phenomenon is captured by the shape factor m obtained from experimental data [18].

References

[1] UNFCCC. Report of the Conference of the Parties on its twenty-first session. Bonn, Germany: United Nations Framework Convention on Climate Change; 2016.

[2] Verhelst S. Recent progress in the use of hydrogen as a fuel for internal combustion engines. Int J Hydrog Energy 2014;39:1071–85. https://doi.org/10.1016/j.ijhydene.2013.10.102.

[3] White C, Steeper R, Lutz A. The hydrogen-fueled internal combustion engine: a technical review. Int J Hydrog Energy 2006;31:1292–305. https://doi.org/10.1016/j.ijhydene.2005.12.001.

[4] Verhelst S, Wallner T. Hydrogen-fueled internal combustion engines. Prog Energy Combust Sci 2009;35:490–527. https://doi.org/10.1016/j.pecs.2009.08.001.

[5] Kahraman E, Cihangir Ozcanlı S, Ozerdem B. An experimental study on performance and emission characteristics of a hydrogen fuelled spark ignition engine. Int J Hydrog Energy 2007;32:2066–72. https://doi.org/10.1016/j.ijhydene.2006.08.023.

[6] Zaccardi J-M, Pilla G. Hydrogen as a Combustion Enhancer for Highly Efficient Ultra-Lean Spark-Ignition Engines. SAE Int J Adv & Curr Prac in Mobility 2020;2(1):401–14.

[7] Hari Ganesh R, Subramanian V, Balasubramanian V, Mallikarjuna JM, Ramesh A, Sharma RP. Hydrogen fueled spark ignition engine with electronically controlled manifold injection: An experimental study. Renew Energy 2008;33:1324–33. https://doi.org/10.1016/j.renene.2007.07.003.

[8] Berckmüller M, Rottengruber H, Eder A, Brehm N, Elsässer G, Müller-Alander G, et al. Potentials of a Charged SI-Hydrogen Engine, 2003, p. 2003-01–3210. https://doi.org/10.4271/2003-01-3210.

[9] Gürbüz H, Akçay İH. Evaluating the effects of boosting intake-air pressure on the performance and environmental-economic indicators in a hydrogen-fueled SI engine. Int J Hydrog Energy 2021;46:28801–10. https://doi.org/10.1016/j.ijhydene.2021.06.099.

[10] Verhelst S, Maesschalck P, Rombaut N, Sierens R. Increasing the power output of hydrogen internal combustion engines by means of supercharging and exhaust gas recirculation. Int J Hydrog Energy 2009;34:4406–12. https://doi.org/10.1016/j.ijhydene.2009.03.037.

[11] Wallner T, Lohse-Busch H. Performance, Efficiency, and Emissions Evaluation of a Supercharged, Hydrogen-Powered, 4-Cylinder Engine, 2007, p. 2007-01–0016. https://doi.org/10.4271/2007-01-0016.

[12] Luo Q-h, Hu J-B, Sun B-G, Liu F-S, Wang Xi, Li C, et al. Experimental investigation of combustion characteristics and NOx emission of a turbocharged hydrogen internal combustion engine. Int J Hydrog Energy 2019;44(11):5573–84.

[13] Lee J, Lee K, Lee J, Anh B. High power performance with zero NOx emission in a hydrogen-fueled spark ignition engine by valve timing and lean boosting. Fuel 2014;128:381–9. https://doi.org/10.1016/j.fuel.2014.03.010.

[14] Prabhukumar G, Nagalingam B, Gopalakrishnan K. Theoretical studies of a spark-ignited supercharged hydrogen engine. Int J Hydrog Energy 1985;10:389–97. https://doi.org/10.1016/0360-3199(85)90065-5.

[15] Rao A, Liu Y, Ma F. Study of NOx emission for hydrogen enriched compressed natural along with exhaust gas recirculation in spark ignition engine by Zeldovich' mechanism, support vector machine and regression correlation. Fuel 2022;318:123577. https://doi.org/10.1016/j.fuel.2022.123577.

[16] Nakata K, Nogawa S, Takahashi D, Yoshihara Y, Kumagai A, Suzuki T. Engine Technologies for Achieving 45% Thermal Efficiency of S.I. Engine SAE Int J Engines 2015;9:179–92. https://doi.org/10.4271/2015-01-1896.

[17] De Bellis V, Malfi E, Bozza F, Kumar D, Serrano D, Dulbecco A, et al. Experimental and 0D Numerical Investigation of Ultra-Lean Combustion Concept to Improve the Efficiency of SI. Engine 2021;3(4):1993–2008.

[18] Sementa P, de Vargas Antolini JB, Tornatore C, Catapano F, Vaglieco BM, López Sánchez JJ. Exploring the potentials of lean-burn hydrogen SI engine compared to

methane operation. Int J Hydrog Energy 2022;47:25044–56. https://doi.org/10.1016/j.ijhydene.2022.05.250.
[19] Gao J, Tian G, Ma C, Zhang Y, Xing S, Jenner P. Lean-burn characteristics of a turbocharged opposed rotary piston engine fuelled with hydrogen at low engine speed conditions. Int J Hydrog Energy 2021;46:1219–33. https://doi.org/10.1016/j.ijhydene.2020.09.167.
[20] Nguyen D, Choi Y, Park C, Kim Y, Lee J. Effect of supercharger system on power enhancement of hydrogen-fueled spark-ignition engine under low-load condition. Int J Hydrog Energy 2021;46:6928–36. https://doi.org/10.1016/j.ijhydene.2020.11.144.
[21] Goldwitz JA, Heywood JB. Combustion Optimization in a Hydrogen-Enhanced Lean-Burn SI Engine, 2005, p. 2005-01–0251. https://doi.org/10.4271/2005-01-0251.
[22] Chen Y, Raine R. Engine Knock in an SI Engine with Hydrogen Supplementation under Stoichiometric and Lean Conditions. SAE Int J Engines 2014;7:595–605. https://doi.org/10.4271/2014-01-1220.
[23] Lee K-J, Huynh TC, Lee J-T. A study on realization of high performance without backfire in a hydrogen-fueled engine with external mixture. Int J Hydrog Energy 2010;35:13078–87. https://doi.org/10.1016/j.ijhydene.2010.04.078.
[24] Li Y, Gao W, Zhang P, Fu Z, Cao X. Influence of the equivalence ratio on the knock and performance of a hydrogen direct injection internal combustion engine under different compression ratios. Int J Hydrog Energy 2021;46:11982–93. https://doi.org/10.1016/j.ijhydene.2021.01.031.
[25] Xu H, Ni X, Su X, Xiao B, Luo Y, Zhang F, et al. Experimental and numerical investigation on effects of pre-ignition positions on knock intensity of hydrogen fuel. Int J Hydrog Energy 2021;46(52):26631–45.
[26] Szwaja S, Bhandary K, Naber J. Comparisons of hydrogen and gasoline combustion knock in a spark ignition engine. Int J Hydrog Energy 2007;32:5076–87. https://doi.org/10.1016/j.ijhydene.2007.07.063.
[27] Dhyani V, Subramanian KA. Experimental investigation on effects of knocking on backfire and its control in a hydrogen fueled spark ignition engine. Int J Hydrog Energy 2018;43:7169–78. https://doi.org/10.1016/j.ijhydene.2018.02.125.
[28] Livengood JC, Wu PC. Correlation of autoignition phenomena in internal combustion engines and rapid compression machines. Symp Int Combust 1955;5:347–56. https://doi.org/10.1016/S0082-0784(55)80047-1.
[29] Keck JC. Turbulent flame structure and speed in spark-ignition engines. Symp Int Combust 1982;19:1451–66. https://doi.org/10.1016/S0082-0784(82)80322-6.
[30] Lindström F, Angstrom H-E, Kalghatgi G, Möller CE. An Empirical SI Combustion Model Using Laminar Burning Velocity Correlations, 2005, p. 2005-01–2106. https://doi.org/10.4271/2005-01-2106.
[31] J.B. H. Internal combustion engine fundamentals. New York: Mcgraw-Hill Education; 2018.
[32] Abbaszadehmosayebi G, Ganippa L. Characterising Wiebe Equation for Heat Release Analysis based on Combustion Burn Factor (Ci). Fuel 2014;119:301–7. https://doi.org/10.1016/j.fuel.2013.11.006.
[33] Salvi BL, Subramanian KA. A novel approach for experimental study and numerical modeling of combustion characteristics of a hydrogen fuelled spark ignition engine. Sustain Energy Technol Assess 2022;51:101972. https://doi.org/10.1016/j.seta.2022.101972.
[34] Eriksson L, Andersson I. An Analytic Model for Cylinder Pressure in a Four Stroke SI Engine, 2002, p. 2002-01–0371. https://doi.org/10.4271/2002-01-0371.
[35] Metghalchi M, Keck JC. Laminar burning velocity of propane-air mixtures at high temperature and pressure. Combust Flame 1980;38:143–54. https://doi.org/10.1016/0010-2180(80)90046-2.
[36] Bradley D, Lawes M, Liu K, Verhelst S, Woolley R. Laminar burning velocities of lean hydrogen–air mixtures at pressures up to 1.0 MPa. Combust Flame 2007;149:162–72. https://doi.org/10.1016/j.combustflame.2006.12.002.
[37] Pareja J, Burbano HJ, Ogami Y. Measurements of the laminar burning velocity of hydrogen–air premixed flames. Int J Hydrog Energy 2010;35:1812–8. https://doi.org/10.1016/j.ijhydene.2009.12.031.
[38] Tse SD, Zhu DL, Law CK. Morphology and burning rates of expanding spherical flames in H2/O2/inert mixtures up to 60 atmospheres. Proc Combust Inst 2000;28:1793–800. https://doi.org/10.1016/S0082-0784(00)80581-0.
[39] Kwon OC, Faeth GM. Flame/stretch interactions of premixed hydrogen-fueled flames: measurements and predictions. Combust Flame 2001;124:590–610. https://doi.org/10.1016/S0010-2180(00)00229-7.
[40] Verhelst S. A study of the combustionin hydrogen-fuelled internal combustion engines. Ghent University; 2005. Ph.D. thesis.
[41] Verhelst S, T'Joen C, Vancoillie J, Demuynck J. A correlation for the laminar burning velocity for use in hydrogen spark ignition engine simulation. Int J Hydrog. Energy 2011;36(1):957–74.
[42] Ravi S, Petersen EL. Laminar flame speed correlations for pure-hydrogen and high-hydrogen content syngas blends with various diluents. Int J Hydrog Energy 2012;37:19177–89. https://doi.org/10.1016/j.ijhydene.2012.09.086.
[43] Gerke U, Steurs K, Rebecchi P, Boulouchos K. Derivation of burning velocities of premixed hydrogen/air flames at engine-relevant conditions using a single-cylinder compression machine with optical access. Int J Hydrog Energy 2010;35:2566–77. https://doi.org/10.1016/j.ijhydene.2009.12.064.
[44] Rakopoulos CD, Kosmadakis GM, Pariotis EG. Evaluation of a combustion model for the simulation of hydrogen spark-ignition engines using a CFD code. Int J Hydrog Energy 2010;35:12545–60. https://doi.org/10.1016/j.ijhydene.2010.09.002.
[45] Woschni G. A Universally Applicable Equation for the Instantaneous Heat Transfer Coefficient in the Internal Combustion Engine, 1967, p. 670931. https://doi.org/10.4271/670931.
[46] Krishnanunni J, Bhatia D, Das LM. Experimental and modelling investigations on the performance and emission characteristics of a single cylinder hydrogen engine. Int J Hydrog Energy 2017;42:29574–84. https://doi.org/10.1016/j.ijhydene.2017.10.018.
[47] Lee J, Park C, Bae J, Kim Y, Choi Y, Lim B. Effect of different excess air ratio values and spark advance timing on combustion and emission characteristics of hydrogen-fueled spark ignition engine. Int J Hydrog Energy 2019;44:25021–30. https://doi.org/10.1016/j.ijhydene.2019.07.181.
[48] Knop V, Benkenida A, Jay S, Colin O. Modelling of combustion and nitrogen oxide formation in hydrogen-fuelled internal combustion engines within a 3D CFD code. Int J Hydrog Energy 2008;33:5083–97. https://doi.org/10.1016/j.ijhydene.2008.06.027.
[49] ANSYS Chemkin 2021.
[50] Li J, Zhao Z, Kazakov A, Dryer FL. An updated comprehensive kinetic model of hydrogen combustion. Int J Chem Kinet 2004;36:566–75. https://doi.org/10.1002/kin.20026.
[51] Eriksson L, Sivertsson M. Calculation of Optimal Heat Release Rates under Constrained Conditions. SAE Int J Engines 2016;9:1143–62. https://doi.org/10.4271/2016-01-0812.
[52] Stokes J, Lake TH, Osborne RJ. A Gasoline Engine Concept for Improved Fuel Economy -The Lean Boost System, 2000, p. 2000-01–2902. https://doi.org/10.4271/2000-01-2902.
[53] Diggs DR. Effect of Combustion Time on Knock in a Spark-Ignition Engine, 1953, p. 530242. https://doi.org/10.4271/530242.
[54] Kneifel A, Buri S, Velji A, Spicher U, Pape J, Sens M. Investigations on Supercharging Stratified Part Load in a Spray-Guided DI SI Engine. SAE Int J Engines 2008;1:171–6. https://doi.org/10.4271/2008-01-0143.
[55] Luo Q-h, Hu J-B, Sun B-G, Liu F-S, Wang Xi, Li C, et al. Effect of equivalence ratios on the power, combustion stability and NOx controlling strategy for the turbocharged hydrogen engine at low engine speeds. Int J Hydrog Energy 2019;44(31):17095–102.
[56] Oikawa M, Kojiya Y, Sato R, Goma K, Takagi Y, Mihara Y. Effect of supercharging on improving thermal efficiency and modifying combustion characteristics in lean-burn direct-injection near-zero-emission hydrogen engines. Int J Hydrog Energy 2022;47:1319–27. https://doi.org/10.1016/j.ijhydene.2021.10.061.
[57] Jeeragal R, Subramanian KA. Experimental Investigation for NOx Emission Reduction in Hydrogen Fueled Spark Ignition Engine Using Spark Timing Retardation, Exhaust Gas Recirculation and Water Injection Techniques. J Therm Sci 2019;28:789–800. https://doi.org/10.1007/s11630-019-1099-3.